The Final Months of Massive Star Evolution from the Circumstellar Environment around SN Ic 2020oi

Keiichi Maeda[1] , Poonam Chandra[2] , Tomoki Matsuoka[1] , Stuart Ryder[3,4] , Takashi J. Moriya[5,6] ,
Hanindyo Kuncarayakti[7,8] , Shiu-Hang Lee[1] , Esha Kundu[9] , Daniel Patnaude[10] , Tomoki Saito[11], and
Gaston Folatelli[12,13,14]

[1] Department of Astronomy, Kyoto University, Kitashirakawa-Oiwake-cho, Sakyo-ku, Kyoto, 606-8502. Japan; keiichi.maeda@kusastro.kyoto-u.ac.jp
[2] National Centre for Radio Astrophysics, Tata Institute of Fundamental Research, Ganeshkhind, Pune 411007, India
[3] Department of Physics and Astronomy, Macquarie University, NSW 2109, Australia
[4] Macquarie University Research Centre for Astronomy, Astrophysics & Astrophotonics, Sydney, NSW 2109, Australia
[5] National Astronomical Observatory of Japan, National Institutes of Natural Sciences, 2-21-1 Osawa, Mitaka, Tokyo 181-8588, Japan
[6] School of Physics and Astronomy, Faculty of Science, Monash University, Clayton, Victoria 3800, Australia
[7] Tuorla Observatory, Department of Physics and Astronomy, FI-20014 University of Turku, Finland
[8] Finnish Centre for Astronomy with ESO (FINCA), FI-20014 University of Turku, Finland
[9] International Centre for Radio Astronomy Research, Curtin University, Bentley, WA 6102, Australia
[10] Smithsonian Astrophysical Observatory, Cambridge, MA 02138, USA
[11] Nishi-Harima Astronomical Observatory, Center for Astronomy, University of Hyogo, 407-2 Nishigaichi, Sayo, Sayo, Hyogo 679-5313, Japan
[12] Instituto de Astrofísica de La Plata (IALP), CONICET, Argentina
[13] Facultad de Ciencias Astronómcas y Geofísicas, Universidad Nacional de La Plata, Paseo del Bosque, B1900FWA, La Plata, Argentina
[14] Kavli Institute for the Physics and Mathematics of the Universe (WPI), The University of Tokyo, Institutes for Advanced Study, The University of Tokyo, 5-1-5
Kashiwanoha, Kashiwa, Chiba 277-8583, Japan

Abstract

We present the results of Atacama Large Millimeter/submillimeter Array (ALMA) band 3 observations of the nearby type Ic supernova (SN) 2020oi. Under the standard assumptions on the SN-circumstellar medium (CSM) interaction and the synchrotron emission, the data indicate that the CSM structure deviates from a smooth distribution expected from the steady-state mass loss in the very vicinity of the SN ($\lesssim 10^{15}$ cm), which is then connected to the outer smooth distribution ($\gtrsim 10^{16}$ cm). This structure is further confirmed through the light-curve modeling of the whole radio data set as combined with the previously reported data at lower frequency. Because this is an explosion of a bare carbon-oxygen (C+O) star with a fast wind, we can trace the mass-loss history of the progenitor of SN 2020oi in the final year. The inferred nonsmooth CSM distribution corresponds to fluctuations on the subyear timescale in the mass-loss history toward the SN explosion. Our finding suggests that the pre-SN activity is likely driven by the accelerated change in the nuclear burning stage in the last moments just before the massive star's demise. The structure of the CSM derived in this study is beyond the applicability of the other methods at optical wavelengths, highlighting the importance and uniqueness of quick follow-up observations of SNe by ALMA and other radio facilities.

1. Introduction

A core-collapse supernova (CCSN) is an explosion of a massive star following the exhaustion of nuclear fuel and the subsequent core collapse (Langer 2012). An increasing opportunity of an early discovery of new SNe and quick follow-up observations at optical wavelengths has opened up a new window to study the nature of the circumstellar medium (CSM) in the vicinity of SNe, which is then translated into the nature of the mass-loss history and pre-SN activity just before the explosion. This investigation has revealed that a large fraction of SNe II have a dense CSM that extends up to a few $\times 10^{15}$ cm, which is frequently termed the "confined CSM" (Gal-Yam et al. 2014; Khazov et al. 2016; Yaron et al. 2017; Förster et al. 2018). If the mass-loss velocity is $v_w \sim 10\,\mathrm{km\,s^{-1}}$ for the extended progenitors of SNe II (mainly red supergiants; RSGs; Smith 2014; Moriya et al. 2017), this confined CSM must have been created by the pre-SN activity in the last ~ 30 yr, with a corresponding mass-loss rate of $\sim 10^{-3}\,M_\odot\,\mathrm{yr^{-1}}$ (Groh 2014; Morozova et al. 2015; Moriya et al. 2017; Yaron et al. 2017; Förster et al. 2018). This is much higher than the

usual mass-loss rate (Smith 2014) derived from the outer CSM distribution ($\sim 10^{-7}$–$10^{-8}\,M_\odot\,\mathrm{yr^{-1}}$; Yaron et al. 2017).

As another piece of evidence for the pre-SN activity, detection of pre-SN outbursts has been reported (Pastorello et al. 2007; Ofek et al. 2013, 2014; Smith et al. 2014; Strotjohann et al. 2021) for rare classes of CCSNe (Li et al. 2011), i.e., SNe IIn and Ibn, showing strong signatures of the SN-CSM interaction in the optical. However, the nature of their progenitor stars has not been well determined (Moriya et al. 2014; Moriya & Maeda 2016). It is not clear if the pre-SN activity observed for these SNe is representative of the massive star evolution.

The mechanism leading to the pre-SN activity at the end of the stellar life has not been clarified. A popular suggestion is that this may be related to the rapidly increasing energy generation by progressively more advanced nuclear burning stages. This final phase may not be represented by a classical "static" stellar evolution theory (Arnett & Meakin 2011; Smith & Arnett 2014), which might underestimate the nuclear energy generation. Furthermore, the generated energy in the core can exceed the hydrostatic limit, and it may be tunneled toward the

envelope as a wave (Quataert & Shiode 2012; Fuller 2017). The envelope may then dynamically respond to the core evolution (Ouchi & Maeda 2019; Morozova et al. 2020). The rapid core evolution may also be coupled with the envelope through the angular momentum transport and could induce the pre-SN mass loss (Aguilera-Dena et al. 2018). None of these possible processes have been taken into account in classical stellar evolution theory.

The core evolution is accelerated toward the formation of the iron core. The mass-loss history in the last $\sim$10–100 yr previously investigated for SNe II corresponds to the carbon-burning stage, which lasts from $\sim$1,000 to $\sim$10 yr before the SN explosion (Langer 2012; Fuller 2017). To understand the origin of the pre-SN final activity, it is desirable to approach the end of the stellar life more closely; neon burning commences only a few years before the explosion, and oxygen burning is activated in the final year.

The so-called stripped envelope SNe (SESNe; Filippenko 1997) provide a good opportunity here. SESNe include SNe Ib from a He star progenitor and SNe Ic from a C + O star progenitor (Langer 2012). The typical mass-loss wind velocity of the SESN progenitors is $v_{\rm w} \sim 1,000\,{\rm km\,s^{-1}}$ (Chevalier & Fransson 2006; Crowther 2007; Smith 2014); CSM at $\sim 10^{15}$ cm must then have been ejected by a progenitor star at $\sim$0.3 yr before the explosion. Given the high wind velocity, the expected CSM density would not be sufficiently high to leave a strong trace in the optical (which is further discussed in Section 5).

Indeed, the "flash" spectroscopy within a few days has mostly been limited to SNe II (Shivvers et al. 2015; Khazov et al. 2016; Yaron et al. 2017; Bruch et al. 2021). An exception is SN IIb 2013cu (Gal-Yam et al. 2014), which represents a transitional object between SNe II and SNe Ib/c. However, the analyses of its flash spectra indicate that the mass-loss velocity of the progenitor is $v_{\rm w} \lesssim 100\,{\rm km\,s^{-1}}$ and most likely $\sim$30 km s^{-1} (Groh 2014; Gräfener & Vink 2016). The progenitor is thus more consistent with the one with an extended H-rich envelope, rather than a genuine He star, being similar to SN IIb 2011dh as a representative case (Maund et al. 2011; Bersten et al. 2012). The other exceptions are SN Ic 2014ft, for which a dense and confined H-poor CSM was inferred from a flash spectrum (De et al. 2018), and broad-lined SN Ic 2018gep, for which the pre-SN activity was inferred from its precursor emission (Ho et al. 2019). SNe Ic 2014ft and 2018gep are peculiar outliers, however, and their progenitor evolution is unlikely to be representative of the bulk of SESNe. Furthermore, the evolution of the mass-loss rate in the final few years has not been quantified in detail for these SESNe.

A few examples exist, e.g., SN Ib 2004dk (Pooley et al. 2019; Balasubramanian et al. 2021), SN Ib 2014C (Anderson et al. 2017; Margutti et al. 2017; Tinyanont et al. 2019), SN Ic 2017dio (Kuncarayakti et al. 2018), and SN Ib 2019oys (Sollerman et al. 2020), where the ejecta of a C + O/He progenitor interact with dense CSM to produce strong emissions either in the optical or in the radio, or both. However, the dense CSM in these SNe was found to be located at $\gtrsim 10^{16}$ cm. This relatively distant CSM should not be created by the pre-SN activity in the last few years. Indeed, they might reflect a rare channel in the binary evolution (Ouchi & Maeda 2017; Kuncarayakti et al. 2018), while the bulk of SESNe are thought to experience the binary interaction at much earlier times (Yoon 2017; Fang et al. 2019). It is necessary to trace the CSM distribution of SNe Ib/c at $\lesssim 10^{15}$ cm to probe the evolution of a massive star in the last few years, which has been challenging so far at optical wavelengths, however. The nature of CSM within $\sim 10^{15}$ cm has been largely unexplored for SNe Ib/c.

This makes radio observation a unique tool, through the synchrotron emission that is exclusively created by the SN-CSM interaction (Björnsson & Fransson 2004; Chevalier & Fransson 2006; Maeda 2012; Matsuoka et al. 2019; Horesh et al. 2020). Multiband radio observations for SESNe in the infant phase ($\lesssim$10 days) have been very limited, however, suffering from a lack of wavelength or temporal coverage, especially at high frequency (Berger et al. 2002; Weiler et al. 2002; Soderberg et al. 2010, 2012; Horesh et al. 2013a, 2013b; Kamble et al. 2016; Bietenholz et al. 2021). The situation is similar for broad-lined SNe Ic, for which radio follow-up observation is routinely undertaken (e.g., Corsi et al. 2016). They tend to show that the CSM density at 10^{16} cm is lower than for typical SESNe, except for a few cases (Terreran et al. 2019; Nayana & Chandra 2020), while little is known about the nature of CSM at the scale of $\sim 10^{15}$ cm. While very rapid radio follow-up observations have been conducted for a few broad-lined SNe Ic associated with a long gamma-ray burst (GRB), the physical scale of the CSM probed at a few days after the explosion is already at $\gtrsim$a few$\times 10^{15}$ cm for these GRB-SNe due to the (sub) relativistic ejecta creating the synchrotron emission (Kulkarni et al. 1998).

The best observed case among SESNe so far would be SN IIb 2011dh (Horesh et al. 2013a), but its progenitor has been derived to be an extended star (Maund et al. 2011) with low $v_{\rm w}$. Another good example of quick radio follow-up observation is SN Ib iPTF13bvn, whose progenitor is probably a compact He star (Cao et al. 2013; Folatelli et al. 2016). The radio data, including the data at 100 GHz, were still sparse, however, and limited to the earliest phase (up to $\sim$10 days; Cao et al. 2013), which is not sufficient to characterize the CSM distribution at different scales.

The recent development of high-cadence surveys now allows multiwavelength follow-up observations of SNe in the infant phase (Bellm et al. 2019; Graham et al. 2019). SN Ic 2020oi in the nearby galaxy M100 ($\sim$15 Mpc) was discovered on 2020 January 7, 13:00:54 (UT), in a very infant phase ($\sim$1 day after the putative explosion date; 2020 January 6, MJD 58854.0 $\pm$ 1.5; Förster et al. 2020; Horesh et al. 2020; Siebert et al. 2020; Rho et al. 2021). In this paper, we present the data from our Atacama Large Millimeter/submillimeter Array (ALMA) observations for SN 2020oi (Section 2). We then investigate the nature of the CSM surrounding SN 2020oi using the ALMA band 3 data (at 100 GHz) as combined with the lower-frequency observations presented by Horesh et al. (2020) from 5 GHz to 44 GHz (Section 3). Based on the analyses in Section 3, we further perform detailed light-curve model calculations in Section 4. The results of Sections 3 and 4 show that the CSM structure around SN 2020oi deviates from a single power-law distribution, indicating that the mass-loss characteristics show fluctuations on the subyear timescale toward the SN explosion, as discussed in Section 5. Discussion in Section 5 further includes possible limitations in the present work, other possible explanations, and further details of the treatment of the physical processes involved in the interpretation. The paper is closed in Section 6 with a summary.

Table 1
ALMA Band 3 Measurement of SN 2020oi (100 GHz)

MJD	Phase (Days)	F_ν (with 1σ error) (mJy beam^{-1})
58859.4	5.4	1.300 ± 0.190
58862.4	8.4	1.219 ± 0.084
58872.3	18.3	0.196 ± 0.058
58905.4	51.3	0.115 ± 0.043

Note. The phase is measured from the putative explosion date (MJD 58854.0; Horesh et al. 2020).

2. Observations and Data Reduction

Our ALMA target-of-opportunity observations, as a part of the cycle 7 high-priority program 2019.1.00350.T (PI: KM), have been conducted starting on 2020 January 11 (UT), covering four epochs. The log of the ALMA observations is shown in Table 1. The on-source exposure time is 16–20 minutes per epoch. All the observations were conducted with band 3, with the same spectral setup for all the observations; the central frequency is 100 GHz, composed of four single continuum windows with a bandwidth of 2 GHz each. Potentially strong molecular bands were avoided in setting the spectral windows, e.g., CO $(J = 0 - 1)$. The arrays are in the C-3 configuration, with the baselines $\sim$15–500 m or $\sim$15–783 m. After the image reconstruction as described below, the angular resolutions are $\sim$1″2–1″6, which guarantees the minimum contamination by known sources, including the core of M100; the SN is located 1″3 east and 6″5 north of the center of M100.

The data have been calibrated through the standard ALMA pipeline with CASA version 5.6.1-8. The image reconstruction has been done with additional manual processes with the CASA *tclean* command. We have used the Briggs scheme with a robustness parameter between -0.5 and 0.5 in weighting the visibility prior to imaging. We have also introduced a minimum baseline cut up to $40k\lambda$ to prevent contamination from possible diffuse sources. The final measurements have then been performed by the CASA *imfit* command, which provides consistent values between the integrated source flux density and peak flux density per beam as expected for a point source. The final error includes the error in *imfit*, image rms, and the error in flux calibration. The flux densities are reported in Table 1. The reconstructed images are shown in Figure 1. A radio point source is clearly detected. The source continues to fade during our observations, and thus it is robustly identified as SN 2020oi.

The lower-frequency excellent data sets at 5–44 GHz were taken from Horesh et al. (2020), which were obtained by ATCA, VLA, AMI-LA, and e-MERLIN. In our analysis, we omit the data for which they suspect nearby source contamination. The multiband light curves including these data are shown in Figure 2, and the spectral energy distributions (SEDs) at three epochs are shown in Figure 3.

We have also checked pre-SN ALMA data covering the position of SN 2020oi (proposal IDs: 2013.1.00634S and 2015.1.00978S; Gallagher et al. 2018a, 2018b). We do not detect a point source at the SN location in the continuum emission, with 1σ upper limits of 0.078 mJy (100 GHz) and 0.062 mJy (250 GHz). If we consider dust emission at the SN environment, it should follow the Rayleigh–Jeans tail, and we may further place an upper limit of $\sim$0.01 mJy at 100 GHz, which is negligible compared to the SN emission.

3. Properties of Radio Emission from SN 2020oi

### 3.1. Characteristic Properties of the Synchrotron Emission from SNe

In order to analyze the multiband radio data of SN 2020oi, we summarize the basic properties of the synchrotron emission from SNe in this section. Throughout this section, we focus on the case in which the CSM density distribution is spherically symmetric and follows a single power law ($\rho_{\rm CSM} \propto r^{-s}$), i.e., the standard assumptions that are widely adopted in analyzing the radio data of SNe. We are especially interested in clarifying the prediction for the CSM created by a steady-state wind, i.e., $s = 2$. In addition to the CSM distribution, below we use a specific (and typical) ejecta structure to show some specific values in the expected radio properties, but we emphasize that the values here are not the primary interest; the key issue here is how the expected properties change as a function of time (e.g., the light curve becoming steeper or flatter), and this behavior is independent of the specific details.

The synchrotron emission originating in the SN-CSM interaction is characterized by the spectral index (α) and temporal slope (β) ($L_\nu \propto \nu^\alpha t^\beta$). In the adiabatic regime with $s = 2$, $\alpha = (1\text{-p})/2$ and $\beta = (3m - 3) + (1 - p)/2$, where p is the spectral index in the relativistic electron energy distribution. Here, m expresses the evolution of the shock wave as $R_{\rm SN} \propto t^m$ (Fransson & Björnsson 1998; Björnsson & Fransson 2004; Chevalier & Fransson 2006; Maeda 2012, 2013a), where $R_{\rm SN}$ is the radius at the shock front. For $p = 3$ typically found for SESNe, $\alpha = -1$. The self-similar decelerated shock solution predicts $m = (n - 3)/(n - s)$, where n is the power-law index in the density distribution within the outer SN ejecta ($\rho_{\rm SN} \propto v^{-n}$), and $n \sim 10$ is frequently adopted for SESNe (Chevalier 1982; Chevalier & Fransson 2006). Substituting $p = 3$ and $m = 0.875$ (for $s = 2$) into the above equation, we obtain $\beta = -1.375$.

In the IC cooling regime, adopting $p = 3$, the predicted behaviors are $\alpha = -1.5$ and $\beta = (5m - 5) - 1/2 - \delta$ (Maeda 2013a; after correcting a typo in the reference), where δ approximates the evolution of the bolometric luminosity (i.e., seed photons) as $L_{\rm bol} \propto t^\delta$. If we adopt $m = 0.875$ (to take into account the deceleration) and constant bolometric luminosity (i.e., at the bolometric peak), the expected temporal slope is $\beta = -1.125$. If we instead adopt $m = 1$ (free expansion), then $\beta = -0.5$. Before the peak, $\delta > 0$, and thus the temporal slope is expected to be steeper than the above prediction (due to the increasing number of seed photons). The opposite is true after the bolometric peak ($\delta < 0$).

3.2. Analysis of the Radio Data of SN 2020oi

Figure 2 presents the multiband radio light curves of SN 2020oi. The ALMA light curve after $\sim$10 days follows a behavior similar to that of the light curves in the other wavelengths at $\gtrsim$15 GHz, but with a different flux density level, indicating that SN 2020oi is in the optically thin limit after $\sim$10 days except for the lowest frequency. The ALMA data are unique at $\lesssim$10 days; the SED (Figure 3) shows that SN 2020oi is fully optically thin at 100 GHz even at $\lesssim$10 days, while this is not the case in the lower frequencies (e.g., it is only marginally optically thin at 44 GHz at day 5). This characteristic nature at the high frequency provides a powerful
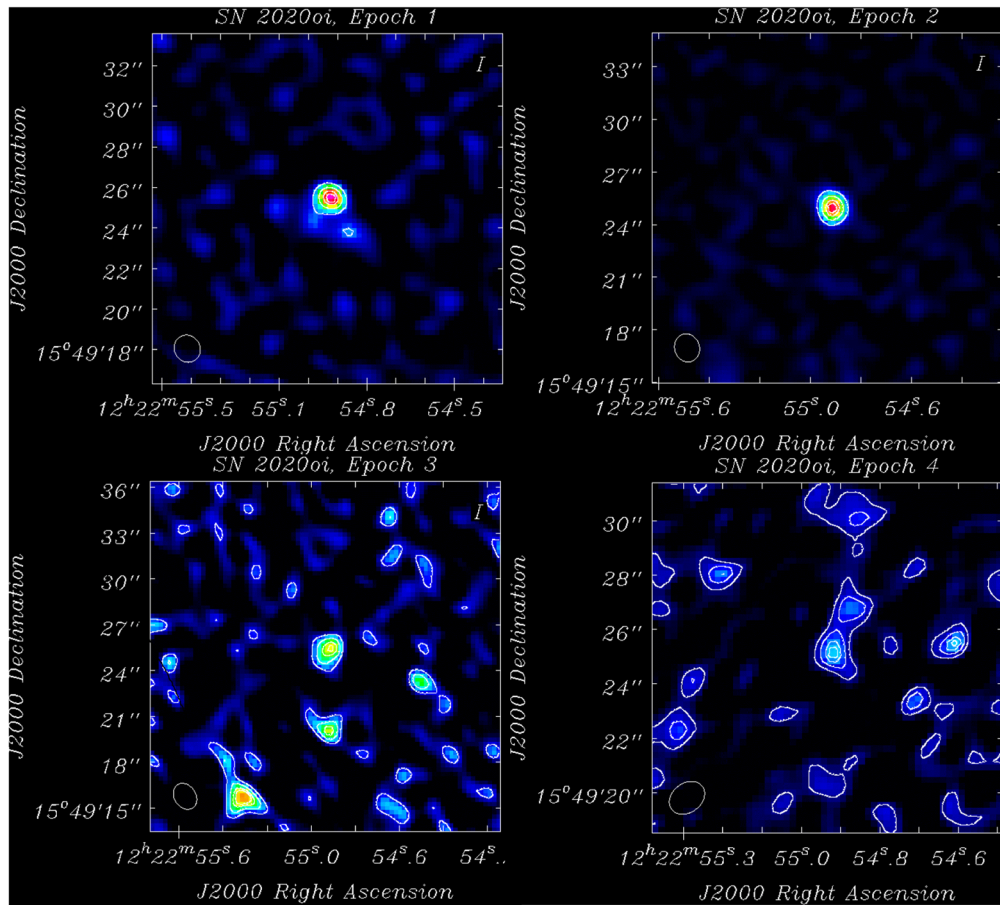
Figure 1. The ALMA band 3 (the central frequency at 100 GHz) images of SN 2020oi, at 5.4 (top left), 8.4 (top right), 18.3 (bottom left), and 51.2 (bottom right) days since the putative explosion date. The color is normalized by the flux density range [0.0 mJy:1.5 mJy] for the earlier two epochs and by [0.0 mJy: 0.3 mJy] for the later two epochs. The contours represent 35%, 60%, 80%, and 90% of the peak flux density. The elliptical beam shape is shown in the bottom left corner in each panel.

tool to investigate the nature of the CSM; the time evolution here should directly reflect the CSM density structure as summarized below (but see Section 5 for caveats and other possibilities).

The radio evolution of SN 2020oi in the optically thin wavelengths (i.e., at 100 GHz for $\lesssim 10$ days and at $\gtrsim 15$ GHz for $\gtrsim 10$ days) can be divided into three characteristic phases (Figure 2): a flat evolution in the early phase ($\lesssim 10$ days), a rapid decay in the intermediate phase (~ 10–40 days), and a slow decay in the late phase ($\gtrsim 40$ days).

As described in Section 3.1, the spectral index of $\alpha \sim -1$ ($f_\nu \propto \nu^\alpha t^\beta$) seen in the late phase is the one predicted for the adiabatic case with the relativistic electron energy distribution with a power-law index of $p \sim 3$ (Björnsson & Fransson 2004; Chevalier & Fransson 2006; Maeda 2013a). For the CSM density distribution described as $\rho_{\rm CSM} \propto r^{-s}$ and $s = 2$ (i.e., steady-state mass loss), the theoretically predicted power-law index in the light-curve decline, in any optically thin band, is $\beta = -1.375$ for the SN ejecta outer layer having a typical distribution of $\rho_{\rm SN}(v) \propto v^{-10}$, where v represents the ejecta velocity coordinate (see Section 3.1). This slope matches the observed light-curve evolution in the late phase ($\gtrsim 40$ days) reasonably well without fine-tuning. These properties in the late phase are typical for radio emission from SESNe at similar phases (Chevalier & Fransson 2006).

In the earlier phases ($\lesssim 40$ days), the optically thin SED passing through the ALMA band is much softer, reaching

$\alpha \sim -1.5$. This spectral slope derived from the multiband data is consistent with the SED within the ALMA band 3, where we see a clear trend of decreasing flux toward the higher frequency; however the individual spectral window data are not very useful to constrain the spectral slope given the limited frequency range, and we rely on the slope derived through the multiband data.[15] The spectral slope is fully consistent with the spectral steepening due to electron cooling, very likely caused by inverse Compton (IC) cooling (Horesh et al. 2020; see Section 5 for further details). The flux at $\lesssim 40$ days is suppressed as compared to a simple extrapolation from the later phase, as expected by the increasing importance of the IC cooling effect toward the earlier epochs.

However, a detailed investigation raises a complication. In Figure 2, the expected range of the slope for the light curve in the IC-dominating regime is shown by the gray region around the bolometric luminosity maximum (i.e., ~ 10 days), covering the free expansion and the decelerated shock cases for the CSM with $s = 2$ and a constant bolometric luminosity for the IC seed photons (Maeda 2013a; see also Section 3.1). The expected slope should be steeper/flatter than this slope before/after the bolometric maximum because of the increasing/decreasing number of the seed photons.

---

[15] The analysis of the individual spectral windows for the third and fourth epochs is even less constraining; the expected flux change within the band is $\sim 10\%$, which is already below the 1σ error in the data obtained by combining all the spectral windows (Table 1).
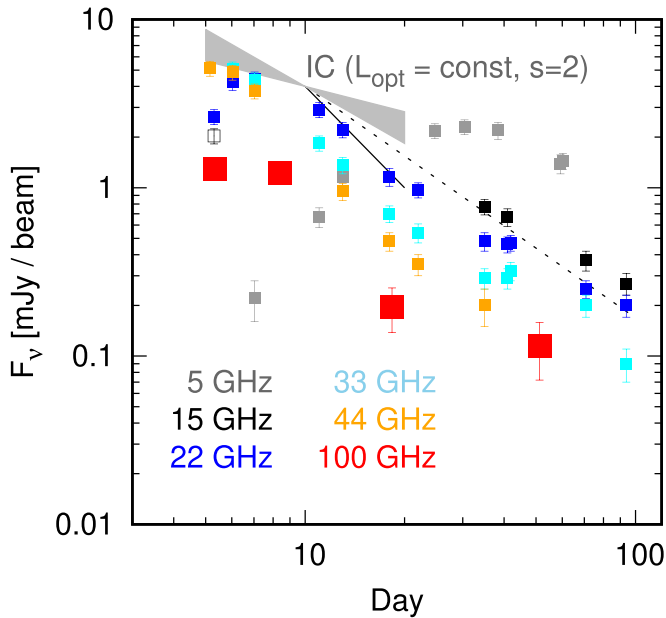
Figure 2. The radio light curves of SN 2020oi. The lower-frequency data are from Horesh et al. (2020). The first point for the 15 GHz data (open square) is in fact measured at 16.7 GHz, and is likely an overestimate of the flux at 15 GHz. The flux densities are shown with 1σ error. A few power-law lines (Section 3.1) are shown that intersect at 10 days (Horesh et al. 2020; Rho et al. 2021, roughly the bolometric maximum date); the dotted black line shows an example of the theoretically expected slope in the adiabatic regime ($\beta = -1.375$), and the gray region represents a range of the expected slope in the IC cooling regime with a constant bolometric luminosity ($\beta = -1.125 \sim -0.5$; Maeda 2013a), adopting the same ejecta and CSM structures as for the adiabatic regime. The solid black line shows $\beta = -2.0$ and roughly fits the slope in the phase immediately after the bolometric maximum.
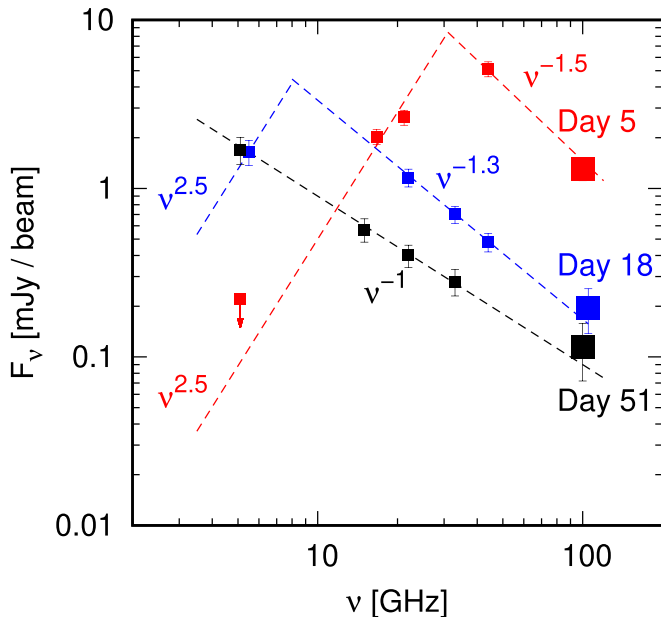
Figure 3. The SEDs at three epochs. The lower-frequency data are from Horesh et al. (2020). The flux densities are shown with 1σ error. The expected spectral slopes are shown for the optically thick regime ($F_\nu \propto \nu^{2.5}$) and in the optically thin regime ($\propto \nu^{-1}$ to $\nu^{-1.5}$).

The observed behavior is opposite to this prediction. In the early phase before the optical peak ($\lesssim 10$ days), the optically thin ALMA data show a flatter evolution than predicted. In the intermediate phase after the optical peak ($\sim 10 - 40$ days), the

observed multiband light curves ($\gtrsim 22$ GHz for the optically thin emission) are steeper. This strongly suggests that the CSM structure in the vicinity of SN 2020oi deviates substantially from a single power-law distribution; a flat distribution in the innermost region and the usual steady-state distribution in the outermost region are connected by a steep density decrease in between.

While the prediction above adopts a specific combination for the CSM density distribution ($s = 2$) and the ejecta density structure ($n = 10$) as motivated by the late-phase behavior, we emphasize that the detail here is not important; for example, if a combination leading to the steeper light-curve evolution (even if this evolution would not explain the late epoch) were adopted, a fit to the optical post-peak decline might be made, but the discrepancy in the pre-peak would become more significant. The opposite is true if a combination leading to a flat evolution in the intrinsic light curve were adopted. The key point is that the discrepancy from the predicted behavior is in the opposite direction before and after the optical peak, which is not remedied by changing the CSM and ejecta density distribution as long as the single power-law function is adopted.

4. Light-curve Models and the CSM Environment

We further quantitatively investigate the CSM distribution with two-step light-curve model calculations. At the first step (Section 4.1), the multiband synchrotron light curves are computed for a single power-law CSM density structure, and the model is applied to each segment of the light-curve evolution (i.e., the early, intermediate, and late phases) separately. This exercise confirms the need for the nonsmooth CSM distribution. The (approximately) derived CSM structure is then used to directly compute the multiband light curves for an arbitrary (but spherically symmetric) CSM structure in the second step (Section 4.2). We have further modified the input CSM structure for the improvement of the model light curves as compared to the data.

The distance to M100 has been derived to be ~ 14–20 Mpc by various measurements,[16] and we adopt 15.5 Mpc. The distance adopted in the previous works for SN 2020oi is in the range of ~ 14–17 Mpc, i.e., 15.5 ± 1.5 Mpc. We may thus consider that the uncertainty on the distance is $\pm 10\%$. Combining rough constraints (i.e., scaling relations) placed on the synchrotron self-absorption frequency, IC cooling frequency, and the optically thin synchrotron emission flux (e.g., Maeda 2012), we estimate that the distance uncertainty translates into the uncertainty on deriving values of the microphysics parameters (ϵ_e and ϵ_B; see Section 4) and the CSM density scale (i.e., the mass-loss rate) at a level of a factor of two. This is sufficiently small for the purpose of the present work. Furthermore, we emphasize that the analysis of the time evolution, which is the main focus of the present work, is essentially independent of the distance uncertainty.

The results from the first-step and second-step models are shown in Figures 4 and 5, respectively. The CSM density distribution thus inferred is shown in Figure 6. We emphasize that these light-curve models are performed to confirm the need for the nonsmooth CSM, and to demonstrate that the CSM structure, qualitatively inferred through the analyses of the key physical processes involved in the synchrotron emission
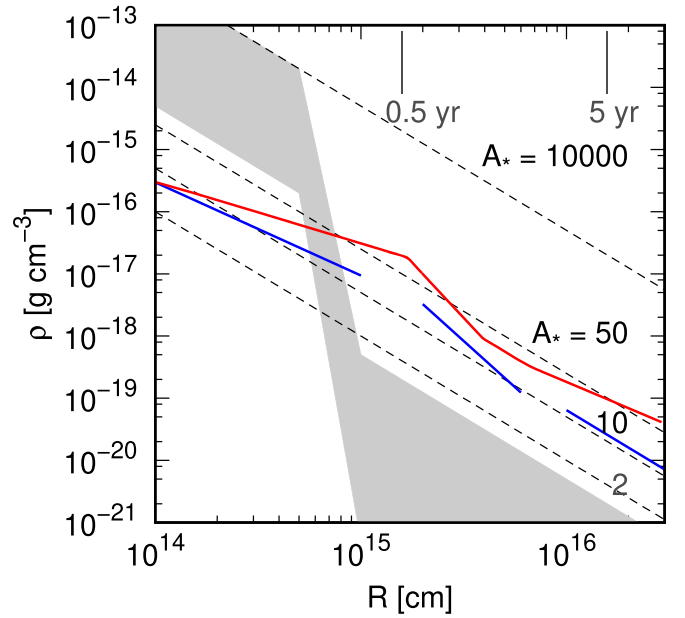
---

[16] https://ned.ipac.caltech.edu
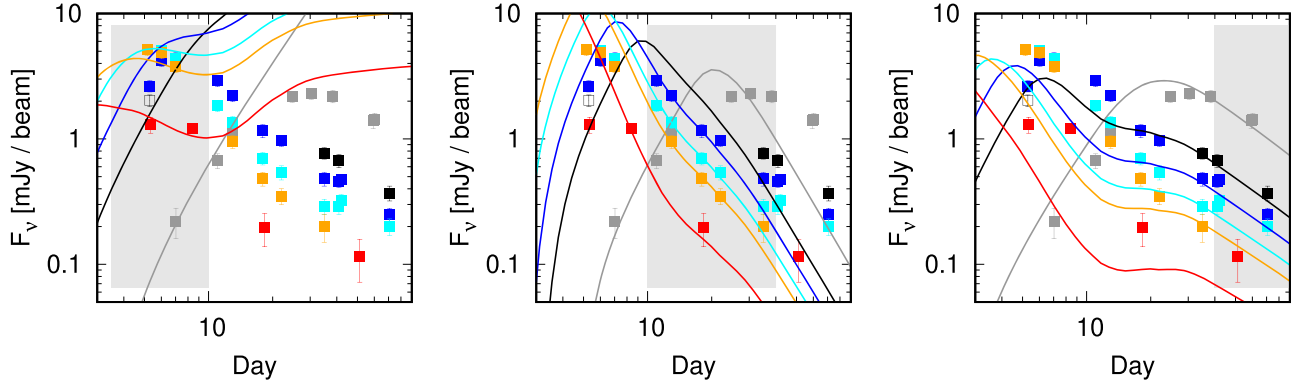
Figure 4. The first-step model light curves compared to the multiband light curves of SN 2020oi. Three models are shown for the early phase with $\rho_{csm} \propto r^{-1.5}$ (left), for the intermediate phase with $\propto r^{-3}$ (middle), and for the late phase with $\propto r^{-2}$ (right), each of which applies only to the limited time window (shaded area in each panel). The color scheme for the data symbols is the same as for Figure 2, and the model curve at each frequency has the same color as the corresponding data symbol.
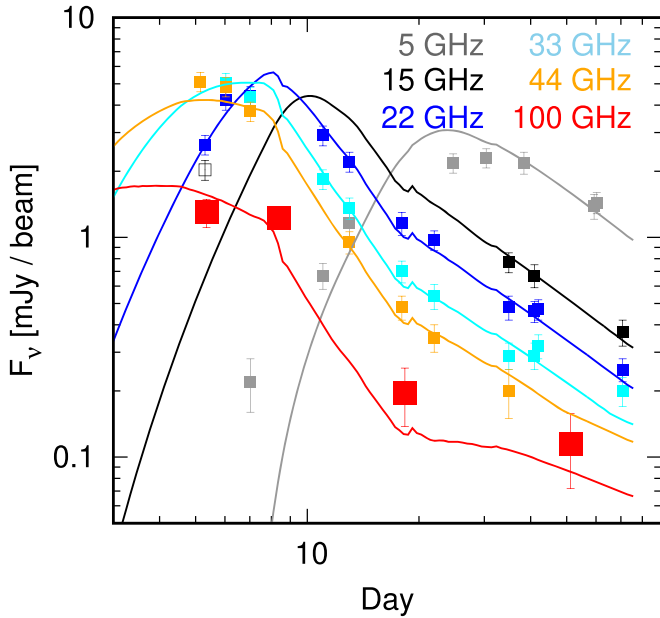
Figure 5. Model light curves as compared to the multiband light curves of SN 2020oi. The model here is computed with the hydrodynamic simulation with the CSM density structure given in Figure 6. The color scheme for the model curves is the same as for the data symbols indicated by the labels.

Figure 6. The circumstellar density distribution inferred for SN Ic 2020oi. The red line is for the final light-curve model (Figure 5), while the blue lines are for the first-step model applied to each time window (Figure 4). For comparison, the fiducial CSM structure derived for SN II 2013fs is shown by the gray shaded area (Yaron et al. 2017). The CSM distributions for steady-state mass loss with a constant velocity (i.e., $\rho_{csm} = 5 \times 10^{11} A_* r^{-2}$, where $A_* = (\dot{M}/10^{-5}\,M_\odot\,\mathrm{yr}^{-1})/(v_w/1{,}000\,\mathrm{km\,s}^{-1})$) are shown for different values of A_*. The corresponding look-back time in the mass-loss history before the explosion is indicated for 0.5 and 5 yr for $v_w = 1{,}000\,\mathrm{km\,s}^{-1}$.

(Section 3), does reproduce the characteristic nature of SN 2020oi seen in the radio data, rather than aiming at accurately deriving the CSM structure.

The initial conditions for both models are the structures of the SN ejecta and the CSM. When a broken power law is adopted for the ejecta density structure, the properties of the SN ejecta are specified by the ejecta mass (M_{ej}), kinetic energy (E_K), and the power-law indices of the inner and outer density distributions in the ejecta velocity coordinate (v); the inner index is set to be 0, and the outer one is denoted as n ($\rho_{SN} \propto v^{-n}$). We adopt $M_{ej} = 1 M_\odot$, $E_K = 10^{51}$ erg, and $n = 10$, which is roughly consistent with the optical light-curve modeling (Rho et al. 2021). We emphasize that the details of these parameters of the ejecta properties are not important for our purpose, which is to demonstrate the need for the nonsmooth CSM as argued in Section 3 in a model-independent way. Changing the ejecta properties could change the overall flux level of the synchrotron emission and thus would affect the overall density scale of the CSM derived by

the comparison between the model and observation; however, it is the temporal "evolution" that matters for the present propose.

After we obtain the properties at the shock front (R_{SN} for the radius and V_{SN} for the velocity), we use the standard formalism that is widely used to simulate the synchrotron emission from the SN-CSM interaction (Fransson & Björnsson 1998; Björnsson & Fransson 2004; Chevalier & Fransson 2006; Maeda 2012; Matsuoka et al. 2019) under the widely used assumptions that the accelerated electrons have a power-law energy distribution (with an index p), and that certain fractions of the energy, ϵ_e and ϵ_B, dissipated at the shock, are transferred to the energy of the relativistic electrons and the amplified magnetic field, respectively. For the cooling processes, we take into account both the synchrotron and IC cooling. For the latter,

we adopt the bolometric light curve presented by Horesh et al. (2020). Synchrotron self-absorption (SSA) is taken into account (Chevalier 1998). Free–free absorption (FFA) is not important in the present study, but for completeness, it is included for the He-rich composition (Matsuoka et al. 2019). For the FFA, the pre-shock CSM temperature is uncertain, and we take $\sim 10^5$ K. The microphysics parameters are p, ϵ_e, and ϵ_B.

4.1. A Single Power-law CSM Distribution for each Epoch

In the first-step model, we adopt a single power-law in the form of $\rho_{csm} = D r^{-s}$ for the CSM density distribution. The parameters here, D and s, are the main targets to derive/ estimate through the radio emission modeling. For the first two phases (up to 40 days), we assume a constant velocity for the shock wave, $V_{SN} = 30,000 \, \mathrm{km \, s^{-1}}$ (Horesh et al. 2020), because the swept-up mass is not sufficient to decelerate the shock wave (Maeda 2013a). For the late epoch, the self-similar solution describing the deceleration of the shock wave is used (Chevalier 1982). We note that the velocity evolution here is adopted for a demonstration purpose; this will be numerically solved in the second-step model.

The situation becomes progressively simpler toward the later epoch, where the effects of absorption and cooling become negligible. We thus start with the model for the late epoch and then move to the earlier epochs. The model light curves are shown in Figure 4, and the density structure used in the model is shown in Figure 6.

The right panel of Figure 4 shows the model applied to the late phase. We adopt $s = 2$ for the CSM structure. For the microphysics parameters, we adopt $p = 3$, $\epsilon_e = 0.01$, and $\epsilon_B = 0.005$ (see also Section 5). These parameters are consistent with those obtained for SN IIb 2011dh by a combined analysis of radio and X-ray data (Maeda 2012; Maeda et al. 2014). The same model extended to the early phase (unshaded region in the same panel of Figure 4), however, illustrates the problems mentioned in Section 3. It is clear that IC cooling is at work, but the temporal evolution is not recovered with $s = 2$.

The need for the steeper density gradient for the intermediate phase is thus clear. The middle panel of Figure 4 shows our model for this phase, with $s = 3$ instead of $s = 2$. The model explains the data reasonably well for ~ 10–40 days. This model again has a problem if it were further extended down to the earlier phase ($\lesssim 10$ days). For example, the ALMA data readily reject the applicability of the same CSM structure before ~ 10 days; it should already be in the optically thin regime (Figure 3), and the steep density distribution results in a too rapid decay.

Therefore we have introduced a flat density structure in the innermost CSM. The left panel of Figure 4 shows the model with $s = 1.5$. The model can explain the increasing trend in the lower-frequency bands and the flat evolution in the higher-frequency bands, and the spectral index is largely consistent with the data.

The microphysics parameters are set identical in the models for the different phases. The electron energy distribution, $p \sim 3$, is robust; the combination of this with the simplest CSM with $s = 2$ naturally explains the late-phase light curves. This is typical for SESNe in similar phases (Chevalier & Fransson 2006). We then have basically three parameters to characterize the radio emission: ϵ_e, ϵ_B, and the CSM density. We have at least three independent observational constraints:

the effect of the SSA (in the early phase), the effect of the IC cooling (in the intermediate phase), and the optically thin flux (in the late phase). Therefore the model parameters are not seriously degenerate. In any case, the exact values of ϵ_e and ϵ_B are not the main focus in the present paper; our main interest in the present work is the temporal evolution of the radio properties, which is then translated into the CSM radial distribution. It is largely insensitive to the values of these parameters (as long as they are constant in time; see Section 5).

4.2. A Detailed Modeling with the Nonsmooth CSM Distribution

As a second step, we have performed a more detailed analysis by numerically solving the evolution of the shock wave for a nonsmooth CSM density distribution. The hydrodynamic evolution is solved using the supernova explosion code (SNEC; Morozova et al. 2015).[17] The simulation provides the shock evolution, i.e., R_{SN} and V_{SN}. The information is then used to compute the synchrotron emission. The SN ejecta properties and the microphysics parameters are set as in the first-step model. An exception is the FFA, for which we changed the pre-shock temperature to see if improvement can be obtained, and the final value we adopt is 2×10^5 K. As another modification, we have introduced a flattening of the electron energy distribution to $p = 2.1$ above the Lorentz factor 300, where the electrons have sufficiently high energy to be further efficiently accelerated (Maeda 2013b); this slightly enhances the late-time high-frequency emission and provides a better agreement with the data.

The CSM density distribution obtained in the first step is used as an initial guess in the second step. The two models do not necessarily agree; the hydrodynamic evolution adopted in the first step is much less accurate, given the deviation of the CSM structure from a single power-law distribution. Therefore we have further tuned the input CSM structure. The result of this exercise is shown in Figures 5 and 6. This detailed model confirms the robustness of the physical interpretation and constraints provided in a model-independent way (Section 3) and by the first-step model (Section 4.1), and it explains the multiband light curves of SN Ic 2020oi reasonably well.

5. Discussion

5.1. The Mass-loss History and the Implications for the Pre-SN Activity

Figure 6 shows the comparison of the CSM structures derived for SN Ic 2020oi in this work and for a representative SN II inferred from the optical data (Yaron et al. 2017). The present work probes the CSM distribution at $\sim 10^{15}$ cm, similar to the previous works for SNe II. However, the corresponding look-back time in the mass-loss history is different; we are able to reach a look-back time of $\lesssim 1$ yr for SN Ic 2020oi. In Figure 7, the CSM density as a function of radius is converted into the mass-loss rate as a function of the pre-SN look-back time assuming a constant mass-loss wind velocity (adopting $v_w = 1,000 \, \mathrm{km \, s^{-1}}$ for SN Ic 2020oi and $10 \, \mathrm{km \, s^{-1}}$ for SN II 2013fs).

The timing in the changes in the mass-loss property derived here roughly corresponds to the transitions in the nuclear

_____
[17] https://www.stellarcollapse.org/SNEC
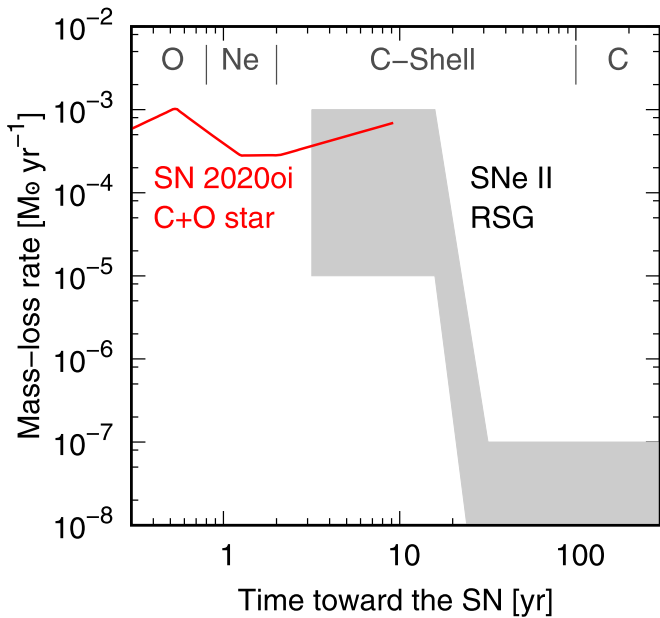
Figure 7. The mass-loss history inferred for SN Ic 2020oi. The CSM density distributions are converted into the mass-loss history, assuming $v_w = 1{,}000$ km s^{-1} for SN Ic 2020oi (red line) and 10 km s^{-1} for SN II 2013fs (gray shaded area). The change in the pre-SN nuclear burning stage is indicated at the top for a star with an initial main-sequence mass of $\sim 15\,M_\odot$ (Fuller 2017).

burning stages; from carbon to neon burning, and then from neon to oxygen burning (Langer 2012; Fuller 2017). The change in the pre-SN nuclear burning stage is indicated in Figure 7 for a star with an initial main-sequence mass of $\sim 15\,M_\odot$ (Fuller 2017). The main-sequence mass for SN 2020oi is suggested to be $\sim 13\,M_\odot$ by Rho et al. (2021) through the optical light-curve model, and the timescale for the advanced burning stages is similar. A somewhat lower progenitor mass ($\sim 9.5\,M_\odot$) has been suggested by Gagliano et al. (2021) through a similar approach; the timescale for the advanced burning stages is then longer by a factor of about two than is shown in Figure 7 (Jones et al. 2013). As an extreme case, the timescale for the advanced burning stages is shorter by a factor of a few for a $25\,M_\odot$ star than for a $15\,M_\odot$ star (Limongi et al. 2000). In summary, regardless of the progenitor mass, the expected timescale for the advanced burning stages fits the timescale we have derived. The "confined CSM" derived for SNe II may also correspond to the transition from the carbon core burning to the shell burning.

These findings suggest that the change in the mass-loss properties in the final evolution of massive stars is likely driven by the change in the nuclear burning stage. Because the timescale here is much shorter than the thermal timescale of a progenitor C + O star ($\sim 1{,}000$ yr), the whole star should respond dynamically to the change in the nuclear burning stage in the core (Ouchi & Maeda 2019; Morozova et al. 2020). This therefore creates the need for a new generation of stellar evolution theory to fully understand the final evolution beyond the classical quasi-static theory.

We note that it is also possible that the change in the mass-loss behavior is driven by the change in mass-loss velocity rather than by the change in mass-loss rate. This would not change our main conclusion because it would also indicate that the characteristic timescale for the pre-SN activity is one year at

most, overlapping with the nuclear burning timescale at the end of the stellar life.

A comparison between SESNe and SNe II in the derived mass-loss history is intriguing, with the caveat that the difference might also originate in the difference in envelope structure. The derived mass-loss rate for SN Ic 2020oi, assuming $v_w \sim 1{,}000$ km s^{-1}, is 10^{-4}–$10^{-3}\,M_\odot$ yr^{-1}. This is higher than the standard steady-state wind for a C + O star ($\sim 10^{-5}\,M_\odot$ yr^{-1}; Crowther 2007), but the fluctuation in the mass-loss rate in the final few years is indeed modest and lower than an order of magnitude. The mass-loss rate in this final burning stage is roughly at the same order as the mass-loss rate derived for SNe II in the less advanced stage at ~ 10 yr before the explosion (Figure 7).

### 5.2. The Effect of IC cooling and Constraints on the Microphysics Parameters

In this section, we provide a qualitative estimate on the effect of the IC cooling. This is used to check the consistency of the microphysics parameters adopted in Section 4. In the following, the values mentioned for some physical quantities are used only for an order-of-magnitude estimate, as is frequently adopted from the results from the light-curve modeling (Section 4). Note that these values are not assumed in the light-curve models in Section 4.

The ratio of the synchrotron cooling timescale ($t_{\rm syn}$) and the IC cooling timescale ($t_{\rm IC}$) is roughly expressed as follows: $t_{\rm syn}/t_{\rm IC} \sim 65 B^{-2} L_{\rm bol,42} R_{15}^{-2}$, where B is the amplified magnetic field strength in Gauss, $L_{\rm bol,42}$ is the bolometric luminosity in 10^{42} erg s^{-1}, and $R_{15} = R_{\rm SN}/10^{15}$ cm (Björnsson & Fransson 2004; Maeda 2013a). At the bolometric peak (~ 10 days), $L_{\rm bol,42} \sim 2$ (Horesh et al. 2020; Rho et al. 2021), and we may take $R_{15} \sim 2$ for $V_{\rm SN} \sim 30{,}000$ km s^{-1}. Therefore the IC cooling becomes a dominant cooling process if $B \lesssim 6$ Gauss. Given $B = \sqrt{8\pi \epsilon_B \rho_{\rm csm} V^2}$ with $V \sim 30{,}000$ km s^{-1}, the condition $\epsilon_B \lesssim 0.016(\rho_{\rm csm,-17})^{-1}$ must be satisfied for the IC cooling to dominate the synchrotron cooling. Here $\rho_{\rm csm,-17}$ is the CSM density at $R_{15} \sim 1$ as normalized by 10^{-17} g cm^{-3}, as found in our final result. This is consistent with $\epsilon_B = 0.005$ adopted in our models.

Indeed, in our model (Figure 5), we find $B \sim 2$ Gauss at 10 days. By adopting $B \sim 2$ Gauss and the other characteristic values for SN 2020oi, we obtain the expected luminosity at 100 GHz in the optically thin, IC cooling regime, as $\sim 4 \times 10^{23} n_e$ erg s^{-1} Hz^{-1}, where n_e is the number density of the relativistic electrons and $n_e \sim \epsilon_e \rho_{\rm CSM} V_{\rm SN}^2 / m_e c^2 \sim 600(\epsilon_e/0.01)$ cm^{-3} (Björnsson & Fransson 2004; Maeda 2013a). The observed synchrotron flux at ~ 10 days corresponds to $\sim 2 \times 10^{26}$ erg s^{-1} Hz^{-1} at 100 GHz. Therefore $\epsilon_e \sim 0.01$ is required.

The estimate here shows $\epsilon_e \sim \epsilon_B \sim 0.001$–$0.01$, which is consistent with the values adopted in our model. Figure 8 shows the evolution of the cooling frequencies found in our final model (Section 4.2; Figure 5), showing that the IC cooling does dominate in the model. The deviation from the full equipartition is preferred, confirming the earlier claim (Horesh et al. 2020). We do not require an extremely large deviation as suggested by Horesh et al. (2020), however, which might highlight the importance of the multiwavelength and time-dependent model calculation, including various cooling and absorption processes simultaneously, as we conducted in the present work. In any case, we emphasize that the ratio of ϵ_e and
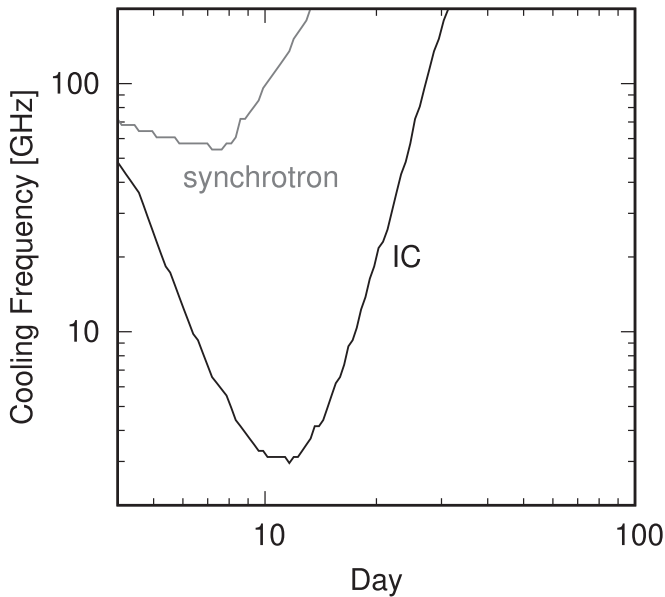
Figure 8. Effect of the IC cooling. The cooling frequency (above which the synchrotron SED becomes steeper) is shown for the IC (black) and for the synchrotron cooling (gray). The figure is for our final model.

ϵ_B can change the overall CSM density scale, but not the normalized CSM density structure as a function of radius, and thus would not affect our main conclusion that a nonsmooth CSM structure is required.

5.3. Other Possible Explanations

In the present work, we have shown that the evolution of the multiband light curves of SN Ic 2020oi, starting in the infant phase, is not explained by a CSM that is distributed smoothly in the radial direction. This conclusion has been reached based on the light-curve analysis and modeling under the standard assumptions that are widely adopted for modeling radio emission from SNe. Especially important assumptions are (1) a constant efficiency of the electron acceleration and magnetic field amplification as a function of time, and (2) a spherically symmetric CSM distribution.

The treatment of the microphysics parameters is phenomenological (not only in this study, but also in the standard analysis for radio SNe) because the details of the particle acceleration are not yet well understood. This is especially the case for the acceleration of electrons to relativistic energy, known as the electron injection problem (see Maeda 2013b for the particular case of an SN-induced shock). However, previous works have been largely successful to explain the behaviors of synchrotron emission from various types of SNe including SESNe under a prescription similar to (or the same as) the present work, assuming constant efficiency for the electron acceleration and magnetic field amplification (e.g., Chevalier & Fransson 2006). Moreover, the validity of this approximation has been confirmed for the particular case of SN IIb 1993J with a more detailed analysis (Fransson & Björnsson 1998). Furthermore, if the possible temporal evolution of the microphysics parameters explains the light curves of SN 2020oi, it would probably require a complicated nonmonotonic evolution as a function of time to explain the characteristic flat-steep-flat evolution seen in the radio light curves of SN 2020oi (Section 3). These considerations suggest that this is probably not the cause of the characteristic evolution seen in SN 2020oi. However, because

the SN radio emission in the infant phase has not been well explored observationally or theoretically, this would require further study.

Asymmetry (i.e., asphericity) may indeed be an important factor to characterize the CSM around SN progenitors. This may especially be the case for SESNe, for which the binary interaction is a popular scenario for the progenitor evolution (Ouchi & Maeda 2017; Yoon 2017), which may create either bipolar-type or disk-like CSM distribution. However, in the standard binary evolution model, the binary mass transfer in the final phase is not important for the compact SESN progenitors including SNe Ic (Ouchi & Maeda 2017; Yoon 2017), and the final mass loss is expected to be dominated by the stellar wind/ activity. In addition, most of the previous works for modeling radio emission from SESNe (or SNe in general) assume spherical symmetry, and they are largely successful to explain the SN radio properties (e.g., Chevalier & Fransson 2006). It is therefore not likely that the characteristic temporal evolution seen in the radio emission from SN 2020oi originated in the asymmetric CSM. Furthermore, the SED of SN 2020oi in each epoch can be described by a single component, with a broken power law describing the optically thick and thin regimes. If the characteristic behavior in the multiband light curves is to be explained by the convolution of multiple CSM components, it will result in a complicated SED at least in a transitional phase. No such evolution is seen in the data. In summary, we conclude that possible asymmetry is probably not the main cause of the characteristic radio behavior seen for SN 2020oi. However, radio emission based on an asymmetric CSM is largely unexplored, and indeed the effect of asymmetric CSM distribution is an interesting topic for various classes of SNe. We postpone further investigation to the future.

As yet another caveat, the question remains what the situation would be like if the synchrotron cooling were indeed to dominate the cooling process. First of all, as shown in Section 5.2 and by Horesh et al. (2020), the IC cooling is very likely the dominant process. This explains the radio light curve and the SED evolution of SN 2020oi under reasonable physical properties (e.g., on the typical CSM density scale). In addition to these arguments, we also emphasize that it would not help to explain the characteristic evolution of SN 2020oi in any case; if a smooth CSM distribution were assumed, the synchrotron cooling frequency would evolve just monotonically as a function of time. It would then never explain the flat-steep-flat evolution of SN 2020oi in its multiband light curves. Therefore we would reach the same conclusion, i.e., the need for a nonsmooth CSM. One may further consider a highly fine-tuned situation in which the synchrotron cooling would dominate in the first 10 days and were then replaced by IC cooling. This would remedy the problem in the early-phase flat evolution, but the problem still remains in the post optical-peak behavior (i.e., the light curve in the cooling regime, but the decreasing cooling effect is steeper than the latter adiabatic phase, in contrast to the expectation).

5.4. Importance of Quick Radio Follow-up Observations

Studying emission properties from infant SESNe provides a unique opportunity to study the mass-loss history in the final phase before the SN explosion; the CSM at $\sim 10^{15}$ cm that can be probed by the SN emission properties corresponds to the final year (or to a time shorter than one year) for SESNe thanks to the expected high mass-loss wind velocity (v_w). The present

study shows that a quick radio follow-up observation is a powerful method that can be more efficient in tracing the nature of the CSM than the optical observations.

Based on the CSM density distribution we have derived for SN 2020oi, we estimate the optical depth of the CSM within $\sim 2 \times 10^{15}$ cm to be $\sim 0.025(\kappa/0.2\,\mathrm{cm}^2\mathrm{g}^{-1}) \ll 1$ for the electron scattering, and thus little trace will be seen at optical wavelengths. This leaves quick radio follow-up observations, especially at high frequency, to catch the optically thin emission as a unique tool for probing the mass-loss history down to the subyear scale before the SN (Matsuoka et al. 2019). Given the decreasing synchrotron flux toward the higher frequency, coupled with the crowded environment in which core-collapse SNe explode, ALMA with its combination of high-sensitivity and high spatial resolution serves as a unique facility.

There is no signature associated with the CSM seen in the optical/UV data of SN 2020oi at $\gtrsim 5$ days (Gagliano et al. 2021; Rho et al. 2021), i.e., the temporal window covered by our radio analysis. This supports the above statement. Gagliano et al. (2021) report a possible enhanced emission in the optical/ UV fluxes at ~ 2.5 days. The CSM density further extrapolated down to the inner region from that derived by the present study would not account for this emission. If the early optical/UV enhancement were associated with the SN-CSM interaction, it would require a huge increase in the mass-loss rate in the final few months before the explosion, at least by an order of magnitude (see the estimate of the optical depth above), which may be associated with the rapid increase in nuclear energy generation toward the final Si burning stage. However, the optical/UV data do not allow us to distinguish between different scenarios for the origin of the early emission, and it may not be associated with the CSM at all (Gagliano et al. 2021). This highlights the importance of rapid radio follow-up observations, especially at high-frequency bands; we need very rapid radio follow-up observations of SNe within the first few days to further constrain the final evolution of massive stars.

6. Summary

While there has been accumulating evidence that a large fraction of massive stars experience dynamic activity toward the end of their lives, the investigation has been largely limited to SNe II using the optical follow-up observations. They are an explosion of an extended progenitor star, and thus their slow mass-loss wind velocity ($v_\mathrm{w} \sim 10\,\mathrm{km\,s}^{-1}$) limits the investigation of the mass-loss history in the final ~ 30 yr. A similar approach for SESNe, especially SNe Ib/c from a compact progenitor star, should allow us to obtain the information on the pre-SN activity in the truly final period within the last year based on the expected high mass-loss wind velocity for these compact progenitors. However, it is expected that the optical data are not sensitive to the properties of the CSM for (canonical) SESNe. An alternative approach is required, and we demonstrate in the present work that quick radio follow-up observations, in particular, those at high frequency, provide a powerful tool for overcoming the difficulty and reaching beyond the current boundary in investigating the final evolution of massive stars.

We have presented our ALMA band 3 (at 100 GHz) observations of a nearby SN Ic 2020oi. Through qualitative (and largely model-independent) analyses and quantitative light-curve model calculations performed on the whole radio

data set as combined with the lower-frequency data (Horesh et al. 2020), we have reconstructed the radial CSM distribution from the very vicinity of the SN ($\lesssim 10^{15}$ cm) to the outer region (a few $\times 10^{16}$ cm), which traces the progenitor activity in its final phase, down to the subyear timescale toward the SN explosion (for an assumed mass-loss velocity of $v_\mathrm{w} = 1{,}000\,\mathrm{km\,s}^{-1}$).

We have argued that the CSM structure, derived under the standard assumptions on the SN-CSM interaction and the synchrotron emission, deviates from the smooth distribution expected from the steady-state mass loss. The radio properties (the SED and the decay slope) of SN 2020oi in the late phase ($\gtrsim 40$ days) are quite typical of SESNe; the smooth CSM structure is roughly approximated by the steady-state wind. However, in the earlier phase ($\lesssim 40$ days), the radio properties are not explained by simply extending the smooth CSM to the inner region. The main argument is the temporal evolution covering the IC cooling phase. The smooth CSM distribution (described by a single power law) predicts that the (optically thin) light curve decays steeply toward the optical peak, then the light curves should be flattened after the peak, and finally, it will eventually become steeper again to reach to the adiabatic regime. This means that the steep-flat-steep evolution is generally expected in a model-independent way. The observed behavior is the opposite, however: the flat-steep-flat evolution is seen, in which the ALMA data play a critical role to identify the flat evolution in the earliest phase. This indicates that the CSM radial distribution follows the flat-steep-flat density distribution from the inner to the outer regions.

The existence of a moderately dense component is thus derived in the very vicinity of the SN ($\lesssim 10^{15}$ cm). Because this is an explosion of a compact C+O star with a fast wind, it indicates that the mass-loss property shows fluctuations on the subyear timescale. This finding suggests that the pre-SN activity is likely driven by the accelerated change in the nuclear burning stage in the last moments just before the massive star's demise.

The structure of the CSM derived in this study is beyond the applicability of other methods at optical wavelengths, highlighting the importance and uniqueness of quick follow-up observations of SNe by ALMA and other radio facilities. The present study provides a proof-of-concept for such an investigation, and we plan to apply similar analyses for a sample of not only SESNe, but SNe II as well. The particular example presented in this paper indicates that the mass-loss rate derived for SN Ic 2020oi in the last few years is likely at a similar level as was derived for SNe II in the last few decades. This may indicate that a common property is likely shared in the final evolution of the progenitors of SESNe and SNe II. The modest fluctuation in the final subyear timescale may also be common, which might simply be missed for SNe II due to the observational difficulty.

However, because the nature of the progenitor stars for SESNe can be diverse, similar analyses need to be performed for a sample of objects. Indeed, SN Ic 2020oi belongs to the population showing the fastest evolution among SESNe (Horesh et al. 2020; Ho et al. 2021; Rho et al. 2021), and it might originate from a progenitor star whose mass is at about the lowest boundary to become an SN Ic (Gagliano et al. 2021). The previous example of the early radio follow-up data for SN Ib iPTF13bvn indicates that the mass-loss rate corresponding to the innermost CSM distribution (up to a few 10^{15} cm) would

only be a few $\times 10^{-5} M_\odot \, \text{yr}^{-1}$ (Cao et al. 2013), which is about an order of magnitude lower than that derived for SN 2020oi in the present work; unfortunately, the data are only available for the early phase up to ~ 10 days for iPTF 13bvn, and thus it is not clear whether iPTF 13bvn also had a nonsmooth CSM distribution. Furthermore, a fair comparison between the innermost CSM densities for the two cases will require a careful analysis and modeling under the same model formalism and treatment of the microphysics parameters. An investigation like this, which not only expands the sample of the quick and well-sampled radio data, but also provides the systematic model analysis, will allow us to understand the nature of the evolution of massive stars in their final phase.

ORCID iDs

Keiichi Maeda https://orcid.org/0000-0003-2611-7269
Poonam Chandra https://orcid.org/0000-0002-0844-6563
Tomoki Matsuoka https://orcid.org/0000-0002-6916-3559
Stuart Ryder https://orcid.org/0000-0003-4501-8100
Takashi J. Moriya https://orcid.org/0000-0003-1169-1954
Hanindyo Kuncarayakti https://orcid.org/0000-0002-1132-1366
Shiu-Hang Lee https://orcid.org/0000-0002-2899-4241
Esha Kundu https://orcid.org/0000-0002-4807-379X
Daniel Patnaude https://orcid.org/0000-0002-7507-8115
Gaston Folatelli https://orcid.org/0000-0001-5247-1486

References

Aguilera-Dena, D. R., Langer, N., Moriya, T. J., & Schootemeijer, A. 2018, ApJ, 858, 115
Anderson, G. E., Horesh, A., Mooley, K. P., et al. 2017, MNRAS, 466, 3648
Arnett, W. D., & Meakin, C. 2011, ApJ, 733, 78
Balasubramanian, A., Corsi, A., Polisensky, E., Clarke, T. E., & Kassim, N. E. 2021, arXiv:2101.07348
Bellm, E. C., Kulkarni, S. R., Graham, M. J., et al. 2019, PASP, 131, 018002
Berger, E., Kulkarni, S. R., & Chevalier, R. A. 2002, ApJL, 577, L5
Bersten, M. C., Benvenuto, O. G., Nomoto, K., et al. 2012, ApJ, 757, 31
Bietenholz, M. F., Bartel, N., Argo, M., et al. 2021, ApJ, 908, 75
Björnsson, C.-I., & Fransson, C. 2004, ApJ, 605, 823
Bruch, R. J., Gal-Yam, A., Schulze, S., et al. 2021, ApJ, 912, 46
Cao, Y., Kasliwal, M. M., Arcavi, I., et al. 2013, ApJL, 775, L7
Chevalier, R. A. 1982, ApJ, 258, 790
Chevalier, R. A. 1998, ApJ, 499, 810
Chevalier, R. A., & Fransson, C. 2006, ApJ, 651, 381
Corsi, A., Gal-Yam, A., Kulkarni, S. R., et al. 2016, ApJ, 830, 42
Crowther, P. A. 2007, ARA&A, 45, 177
De, K., Kasliwal, M. M., Ofek, E. O., et al. 2018, Sci, 362, 201
Fang, Q., Maeda, K., Kuncarayakti, H., Sun, F., & Gal-Yam, A. 2019, NatAs, 3, 434
Filippenko, A. V. 1997, ARA&A, 35, 309
Folatelli, G., Van Dyk, S. D., Kuncarayakti, H., et al. 2016, ApJL, 825, L22
Förster, F., Moriya, T. J., Maureira, J. C., et al. 2018, NatAs, 2, 808
Förster, F., Pignata, G., Bauer, F. E., et al. 2020, Transient Name Server Discovery Report, 2020-67, 1
Fransson, C., & Björnsson, C.-I. 1998, ApJ, 509, 861
Fuller, J. 2017, MNRAS, 470, 1642
Gagliano, A., Izzo, L., Kilpatrick, C. D., et al. 2021, arXiv:2105.09963
Gallagher, M. J., Leroy, A. K., Bigiel, F., et al. 2018a, ApJL, 868, L38
Gallagher, M. J., Leroy, A. K., Bigiel, F., et al. 2018b, ApJ, 858, 90
Gal-Yam, A., Arcavi, I., Ofek, E. O., et al. 2014, Natur, 509, 471
Gräfener, G., & Vink, J. S. 2016, MNRAS, 455, 112
Graham, M. J., Kulkarni, S. R., Bellm, E. C., et al. 2019, PASP, 131, 078001
Groh, J. H. 2014, A&A, 572, L11
Ho, A. Y. Q., Goldstein, D. A., Schulze, S., et al. 2019, ApJ, 887, 169
Ho, A. Y. Q., Perley, D. A., Gal-Yam, A., et al. 2021, arXiv:2105.08811
Horesh, A., Kulkarni, S. R., Corsi, A., et al. 2013b, ApJ, 778, 63
Horesh, A., Sfaradi, I., Ergon, M., et al. 2020, ApJ, 903, 132
Horesh, A., Stockdale, C., Fox, D. B., et al. 2013a, MNRAS, 436, 1258
Jones, S., Hirschi, R., Nomoto, K., et al. 2013, ApJ, 772, 150
Kamble, A., Margutti, R., Soderberg, A. M., et al. 2016, ApJ, 818, 111
Khazov, D., Yaron, O., Gal-Yam, A., et al. 2016, ApJ, 818, 3
Kulkarni, S. R., Frail, D. A., Wieringa, M. H., et al. 1998, Natur, 395, 663
Kuncarayakti, H., Maeda, K., Ashall, C. J., et al. 2018, ApJL, 854, L14
Langer, N. 2012, ARA&A, 50, 107
Li, W., Leaman, J., Chornock, R., et al. 2011, MNRAS, 412, 1441
Limongi, M., Straniero, O., & Chieffi, A. 2000, ApJS, 129, 625
Maeda, K. 2012, ApJ, 758, 81
Maeda, K. 2013a, ApJ, 762, 14
Maeda, K. 2013b, ApJL, 762, L24
Maeda, K., Katsuda, S., Bamba, A., Terada, Y., & Fukazawa, Y. 2014, ApJ, 785, 95
Margutti, R., Kamble, A., Milisavljevic, D., et al. 2017, ApJ, 835, 140
Matsuoka, T., Maeda, K., Lee, S.-H., & Yasuda, H. 2019, ApJ, 885, 41
Maund, J. R., Fraser, M., Ergon, M., et al. 2011, ApJL, 739, L37
Moriya, T. J., & Maeda, K. 2016, ApJ, 824, 100
Moriya, T. J., Maeda, K., Taddia, F., et al. 2014, MNRAS, 439, 2917
Moriya, T. J., Yoon, S.-C., Gräfener, G., & Blinnikov, S. I. 2017, MNRAS, 469, L108
Morozova, V., Piro, A. L., Fuller, J., & Van Dyk, S. D. 2020, ApJL, 891, L32
Morozova, V., Piro, A. L., Renzo, M., et al. 2015, ApJ, 814, 63
Nayana, A. J., & Chandra, P. 2020, MNRAS, 494, 84
Ofek, E. O., Sullivan, M., Cenko, S. B., et al. 2013, Natur, 494, 65
Ofek, E. O., Sullivan, M., Shaviv, N. J., et al. 2014, ApJ, 789, 104
Ouchi, R., & Maeda, K. 2017, ApJ, 840, 90
Ouchi, R., & Maeda, K. 2019, ApJ, 877, 92
Pastorello, A., Smartt, S. J., Mattila, S., et al. 2007, Natur, 447, 829
Pooley, D., Wheeler, J. C., Vinkó, J., et al. 2019, ApJ, 883, 120
Quataert, E., & Shiode, J. 2012, MNRAS, 423, L92
Rho, J., Evans, A., Geballe, T. R., et al. 2021, ApJ, 908, 232
Shivvers, I., Groh, J. H., Mauerhan, J. C., et al. 2015, ApJ, 806, 213
Siebert, M. R., Kilpatrick, C. D., Foley, R. J., & Cartier, R. 2020, Transient Name Server Classification Report, 2020-90, 1
Smith, N. 2014, ARA&A, 52, 487
Smith, N., & Arnett, W. D. 2014, ApJ, 785, 82
Smith, N., Mauerhan, J. C., & Prieto, J. L. 2014, MNRAS, 438, 1191
Soderberg, A. M., Brunthaler, A., Nakar, E., Chevalier, R. A., & Bietenholz, M. F. 2010, ApJ, 725, 922
Soderberg, A. M., Margutti, R., Zauderer, B. A., et al. 2012, ApJ, 752, 78
Sollerman, J., Fransson, C., Barbarino, C., et al. 2020, A&A, 643, A79
Strotjohann, N. L., Ofek, E. O., Gal-Yam, A., et al. 2021, ApJ, 907, 99
Terreran, G., Margutti, R., Bersier, D., et al. 2019, ApJ, 883, 147
Tinyanont, S., Lau, R. M., Kasliwal, M. M., et al. 2019, ApJ, 887, 75
Weiler, K. W., Panagia, N., Montes, M. J., & Sramek, R. A. 2002, ARA&A, 40, 387
Yaron, O., Perley, D. A., Gal-Yam, A., et al. 2017, NatPh, 13, 510
Yoon, S.-C. 2017, MNRAS, 470, 3970